Journal of Histochemistry & Cytochemistry 1–19

DOI: 10.1369/00221554251413643
journals.sagepub.com/home/jhc
Sage

Correlating Stimulated Emission Depletion Microscopy With Fluorescence Lifetime Imaging Microscopy to Study the TIE2 Protein on Kidney Glomerular Podocytes

Iulia-Aneta Dénes, Irina A. Okkelman, Herlinde De Keersmaecker, Pieter Cornillie, Ruslan I. Dmitriev, and Ward De Spiegelaere
Laboratory of Veterinary Morphology, Faculty of Veterinary Sciences (IAD, PC, WS), and Tissue Engineering and Biomaterials Group, Department of Human Structure and Repair (IAO, RID), and Ghent Light Microscopy (GLiM) CORE (IAO, HK, RID, WS), Ghent University, Ghent, Belgium

Summary
The TIE2 transmembrane receptor protein, known for its role in vascular stability and blood vessel remodeling, has primarily been studied in endothelial cells. This receptor has also been found on several non-endothelial cell types including podocytes, although its presence on podocytes remains a matter of debate. Conventional immunofluorescence approaches applied to membrane proteins are often challenged by the strong tissue autofluorescence spanning green and red parts of the electromagnetic spectrum, sample thickness, and the antibody specificity. Here, we used stimulated emission depletion (STED) microscopy, a super-resolution microscopy method, to detect the TIE2 protein in complex biological tissue with a resolution of less than 50 nm. To further confirm the presence of TIE2 on podocytes and to investigate its localization, we used fluorescence lifetime imaging microscopy (FLIM) to more effectively distinguish between nonspecific autofluorescence and specific emission in cleared and antibody-labeled tissue samples. By correlating these two techniques, we mapped the subcellular localization of TIE2 on mouse podocytes and confirmed its presence on the cell surface facing the Bowman's space, albeit at lower expression levels. This study highlights the potential complementary power of STED and FLIM methods and provides additional evidence that the TIE2 receptor is present on podocytes. **(J Histochem Cytochem XX:XXX–XXX, XXXX)**

Keywords
confocal microscopy, FLIM, immunofluorescence, mouse, podocyte, STED, TIE2

Introduction

TIE2, the Tyrosine Kinase with Immunoglobulin and Epidermal Growth Factor Homology Domain-2 receptor, plays a pivotal role in endothelial cell survival and vascular homeostasis, regulating blood vessel integrity and new vessel formation.[1–3] The TIE2 receptor has also been found, albeit at lower levels, on non-endothelial cells such as pericytes, hematopoietic cells, and various cancer cells.[4–8] In the kidney, TIE receptors have been detected in rat and pig podocytes using transmission electron microscopy (TEM). Here as well, TIE expression on podocytes was lower compared with that on glomerular endothelial cells.[9,10] Traditional techniques used to study protein localization, such as TEM and fluorescence microscopy, pose certain limitations. First, immunogold labeling with TEM enables the localization of proteins within cells with high resolution, but this technique is laborious and restricted to very small and thin samples.[11] Second, the specific preprocessing procedures required for TEM can interfere with antibody labeling

Journal of Histochemistry & Cytochemistry

and result in staining artifacts,[12] complicating data interpretation. In contrast, widefield fluorescence microscopy techniques lack the necessary resolution to localize proteins precisely in complex tissues. Relying on fluorescence intensity measurements can also pose problems when the proteins of interest are sparsely expressed or when the signal-to-noise ratio is low due to sample heterogeneity. Furthermore, tissues frequently display intrinsic autofluorescence, derived from endogenous molecules such as flavins, porphyrins, nicotinamide adenine dinucleotide, and their byproducts. Autofluorescence often appears and remains present due to pre- and post-sample preparation and tissue fixation. This complicates accurate signal detection as autofluorescence interferes with the specific fluorescent labeling.[13–15] In addition, nonspecific antibody binding increases background noise and contributes to false-positive signals.[15]

In recent years, the development of new microscopy methods, coupled with sample optical clearing and expansion,[16] has overcome these limitations.

Super-resolution light microscopy methods, such as stimulated emission depletion (STED) microscopy, in conjunction with tissue clearing and expansion techniques,[16] have been demonstrated to be efficacious in localizing specific molecules in tissues at a higher resolution than conventional widefield microscopy.[17–19] Although STED does not reach the resolution of TEM, it surpasses that of conventional microscopy by breaking the diffraction limit and allowing protein localization on the nanometer scale in large specimens (above 200 µm),[16] using similar staining procedures as used in conventional fluorescence microscopy.[17] To address the diffraction limit, which restricts the spatial optical resolution, STED employs a dual-laser approach and simultaneously scans a tissue with an excitation laser and a red-shifted depletion laser, which has the shape of a donut. The depletion laser induces a photophysical phenomenon called STED in the periphery of the diffraction-limited confocal focus, thereby forcing the fluorophores to return to the ground state without emitting a photon. This technique effectively narrows the excitation point, resulting in a sub-50-nm resolution spot.[17,19–21]

Fluorescence lifetime imaging microscopy (FLIM) complements conventional fluorescence intensity detection by measuring the lifetime (or decay time) of a fluorophore (τ). Fluorescence lifetime reflects the time that a fluorophore remains in its excited state before emitting a photon.[22] Unlike intensity-based methods, fluorescence lifetime is an intrinsic property of the fluorophore itself and is thus not affected by such factors as fluorophore concentration, excitation intensity, or photobleaching. Fluorescence lifetime can also reflect the microenvironment of the fluorescent molecule: local pH, viscosity, polarity, and protein–protein interactions can affect the fluorescence lifetime of the measured fluorophores, allowing them to be distinguished in a complex mixture and in a microenvironmental context.[13,22,23] In indirect immunofluorescence methods, autofluorescence and nonspecific binding of secondary antibodies typically exhibit different fluorescence lifetimes compared to specific binding events. FLIM therefore improves image contrast and data reliability by allowing clear discrimination between specific and nonspecific signals within a single image.[13,17,22,24]

In this study, we report STED data describing the localization of the TIE2 receptor on mouse kidney podocytes. We support our findings with FLIM data demonstrating that with a simple analysis strategy, autofluorescence and nonspecific secondary antibody binding to the tissue can be accurately distinguished from low-expressed specific signal. Combining these two techniques can improve spatial resolution and enhance data reliability, particularly in samples where nonspecific binding events present challenges.

Materials and Methods

Tissues and Antibodies

Mouse kidney tissues were kindly donated by the Ghent University Animalarium. All procedures with animals were performed in accordance with the Directive 2010/63/EU adopted by the European Parliament and the Council of the European Union. Mice (Hsd:ICR (CD-1), 4–6 months old) were sacrificed using cervical

Received for publication June 3, 2025; accepted December 19, 2025.

Corresponding Authors:
Ward De Spiegelaere, Laboratory of Veterinary Morphology, Faculty of Veterinary Sciences, Ghent University, Salisburylaan 133, Merelbeke 9820, Belgium.
E-mail: Ward.DeSpiegelaere@UGent.be

Ruslan I. Dmitriev, Tissue Engineering and Biomaterials Group, Department of Human Structure and Repair, Faculty of Medicine and Health Sciences, Ghent University, The Core, C. Heymanslaan 10, Gent 9000, Belgium.
E-mail: Ruslan.Dmitriev@UGent.be

dislocation, according to the protocol approved by the Ghent University Ethics Committee on Animal Testing. Antibodies and stains included the anti-mouse/rat TIE-2 polyclonal goat IgG primary antibody (AF762; R&D Systems, Dublin, Ireland) and wheat germ agglutinin (WGA) conjugated to CF405M (Biotium, Huissen, The Netherlands), secondary donkey anti-goat IgG StarRED 638 (Abberior, Goettingen, Germany), recombinant Mouse Tie-2 Fc Chimera Protein (762-T2; R&D Systems, Dublin, Ireland), rabbit anti-podocin (P0372; Sigma-Aldrich, Schnelldorf, Germany), and its secondary donkey anti-rabbit (A-21207; Thermo Fisher Scientific, Zaventem, Belgium).

Tissue Preparation and Immunolabeling

For tissue clearing and expansion, we used a previously optimized protocol for mouse kidneys by Unnersjö-Jess et al.[16] Briefly, mouse kidneys were fixed in paraformaldehyde (4%, 3 hr) and stored in 70% ethanol (at room temperature). Fixed kidneys were cut into 2- to 3-mm-thick slices and transferred to a 4% acrylamide hydrogel solution overnight at 4C. Subsequently, the hydrogel was polymerized (37C, 3 hr, shaking) and samples were sectioned on a vibratome (100 µm, Oxford Vibratome, Sectioning System Model G, St. Louis, Missouri). Tissue slices were cleared in SDS-boric acid clearing solution for 18 hr (50C), followed by 6 hr (37C). Samples were labeled with the TIE2 primary antibody (20 µg/ml, 37C, 24 hr), followed by WGA and secondary antibody staining (20 µg/ml, 37C, 24 hr) in PBS with 0.1% TritonX-100. Between each step, samples were washed in PBS with 0.1% TritonX-100. For the antibody control samples in which certain antibodies were excluded were kept in the antibody buffer solution (PBS 0.1% TritonX-100) in the same incubation conditions. Before mounting with glass coverslips (thickness no. 1.5) and imaging, samples were immersed in 80% fructose solution (3 hr, room temperature), protected from light. For longer storage (up to 7 days), samples were preserved in the fructose solution at 4C in the dark. The same protocol was used for the costaining of TIE2-podocin or recombinant protein experiments, with the addition that the recombinant protein [100 µg/ml (or 1 part primary antibody to 5 parts recombinant protein)] was first incubated with the primary antibody for 2 hr at room temperature on a shaker in 1× PBS.

An in vitro droplet test using the StarRED and anti-TIE2 antibody was performed and the following conditions were tested: StarRED alone 400 µg/ml and StarRED in the same concentration with anti-TIE2 antibody 50 µg/ml or 100 µg/ml. The antibodies were incubated in PBS 0.1% TritonX-100 for 10 min at room temperature before imaging.

Microscopy

In the workflow, samples were first imaged on the FLIM system and then imaged on the STED system. In both cases, mosaic scans of the tissue were produced, and the glomeruli subjected to analysis were chosen randomly (Fig. 1). The staining protocol allowed consistent penetration of up to 60 µm into the expanded tissue (Fig. 2). For analysis, however, we restricted measurements to the superficial 0 to 20 µm, with 0 being the top of the sample, to minimize depth-dependent intensity variation.

Super-resolution microscopy was performed on a STED microscope (Facility Line, Abberior Instruments, Göttingen, Germany) using a silicon immersion UPLSAPO60XS objective, NA 1.3, WD 0.3 mm (Olympus, Tokyo, Japan) installed on an Olympus IX83 inverted microscope body. A 405 nm CW diode and a 640 nm pulsed diode laser were used to excite WGA and Star RED 638, respectively. Depletion of Star RED 638 was performed by a pulsed 775 nm laser in two dimensions (2D). All pulsed lasers had a repetition rate of 40 MHz. Fluorescence emission was detected by a spectral detection unit using an APD detector (416–526 nm and 650–755 nm emission wavelengths for WGA and Star RED 638, respectively). The image was scanned unidirectionally with 1 line accumulation for the WGA and 20 line accumulations for the Star RED 638. The pixel size and pixel dwell time were set to 30 nm and 5 µs, respectively. The pinhole was set to 1.0 AU (Airy Units). STED images were acquired with the Abberior Lightbox software and analyzed in ImageJ.[25]

FLIM was performed using the Stellaris 8 Falcon FLIM (Leica Microsystems, Diegem, Belgium) inverted microscope, based on DMi8 CS body, equipped with a 405 nm diode laser and white light laser (440–790 nm, 80 MHz), power HyD X and R detectors, HC PL APO 40×/1.25 GLYC CORR CS2, and HC PL APO 63×/1.4 OIL CS2 objectives. WGA was excited with the 405 nm laser (non-pulsed), and intensity images were captured on a HyD S detector between 425 and 479 nm, whereas for StarRED the excitation was set to 645 nm, and fluorescence lifetime measurements were collected using a HyD R detector. The intensity detection range on the HyD R detector was set between 661 and 834 nm. Scanning was performed unidirectionally, with 100 Hz speed and 1 accumulation line. The pixel size was set between 0.081 and 0.241 µm, and the pixel dwell time was 7.68 µs. The pinhole was set to 1.0 AU. FLIM images and phasor plots were acquired and analyzed in LAS X and LAS X FLIM/FCS software (Leica Microsystems).

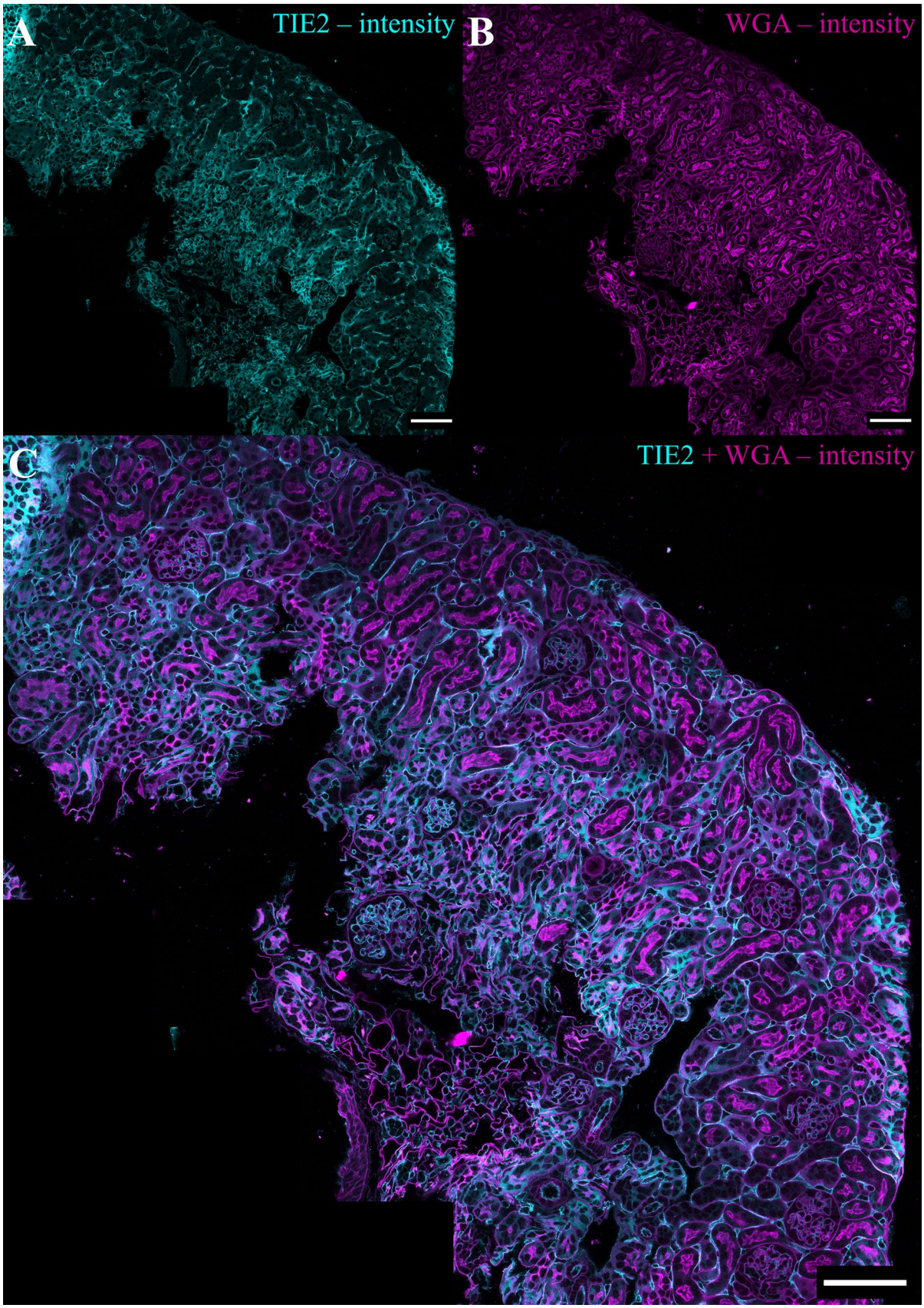

Figure 1. Overview of analyzed kidney tissue using mosaic scan. A: Mosaic scan of TIE2 stain on kidney tissue (intensity image); B: Mosaic scan of Wheat Germ Agglutinin membrane staining on kidney tissue (intensity image); C: Overlay of A and B (intensity image); scale bar 100 µm.

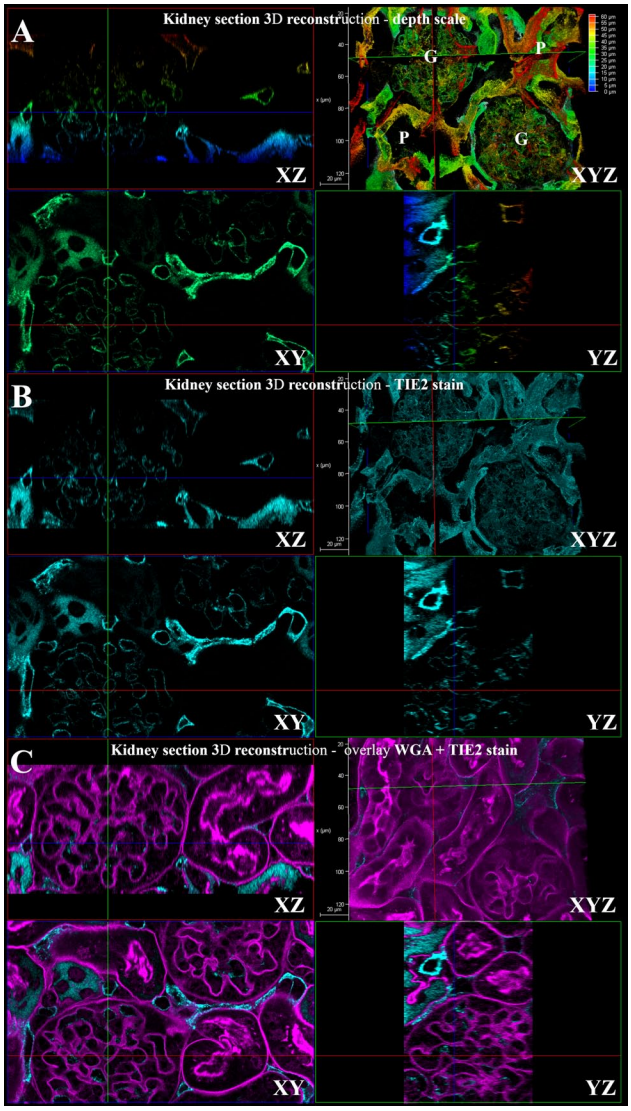

Figure 2. 3D reconstructions of a kidney section. Figure shows 3D intensity reconstruction of the overall organization of two glomeruli (G) and adjacent parenchyma (P) across the depth (Z) of 60 μm; A: 3D reconstruction of the TIE2 stain, presenting image depth scale from 0 μm (blue) toward 60 μm (red). Different panels present the different plane views (XZ, XYZ, XY, YZ); B: 3D reconstruction presenting the TIE2 stain in the same planes as described above; C: 3D reconstruction presenting an overlay image of the WGA membrane stain (magenta) and the TIE2 stain (cyan) in the different planes described above.

Image Analysis

Podocytes were identified based on their localization and position. Within each glomerulum, only the cells located directly at the glomerular periphery and facing the Bowman's space were chosen for analysis, as only podocytes are present at this position, where they fully envelope the glomerular capillaries. To avoid any signal interference emerging from the Z-plane, the analyzed image regions were selected based on the perpendicular alignment of the podocyte bodies and foot processes to the blood vessels.

For STED, confocal images of the WGA membrane stain and 2D-STED images of the TIE2 stain were collected. To quantify intensity profiles across regions of interest (ROIs) in podocytes, images were analyzed with the Clock Scan plugin[26] in ImageJ, ver. 2.3.0.[25] The Clock Scan plugin enables average pixel intensity quantification, both within and right outside the borders of convex-shaped ROI. The protocol collects radial pixel intensity profiles, starting from the center of the ROI toward the predefined border or selected distance outside the ROI. The radial scans represent 100% of the X scale, with 100% being the border of the ROI and 0 being the ROI's center. The ROI radius can be automatically increased so that the measurements also take place outside of the initial ROI borders. Therefore, the X scale can be modified up to 200% and the protocol scans an area outside of the initial ROI, equal to the fraction of the radius provided.[26]

The Clock Scan analysis was performed on manually traced ROIs of the top half of the podocyte cell body, with the X and Y center of the Clock Scan ROI determined automatically by the plugin and a scan limit (fraction of radius) of 1.20 (X scale = 120%). The intensity readouts for both the TIE2 and WGA images were compared at the peak intensity level on a scale of 0% to 120%, with 0% representing the center of the ROI area and 120% representing the border of the ROI. Figure 3 briefly showcases this approach. A total of 28 different podocytes over two experimental replicates were analyzed.

For FLIM phasor and fitting analyses, we used the built-in phasor plot tool and fitting tool of the LAS X FLIM/FCS software (ver. 4.6.1 or later, Leica Microsystems). The phasor plot approach simplifies viewing the lifetime distribution within a two-dimensional (2D) graphical view by converting each image pixel into a point on a 2D plot. Multiple fluorescent species can be distinguished and back-gated onto the image with the aid of integrated tools, such as the circle function or the line function.[27,28] Threshold optimization was performed on the autofluorescence and Star RED secondary antibody controls. For the phasor plot approach, the final filters applied were the following: Median 17, Threshold 27, Harmonic 1, and Pixel binning 1.

The fluorescence lifetime decay curves of the traced ROIs were also fitted using a double-exponential fitting function[29] as fitting data are considered more accurate, but less visual than the phasor plot approach

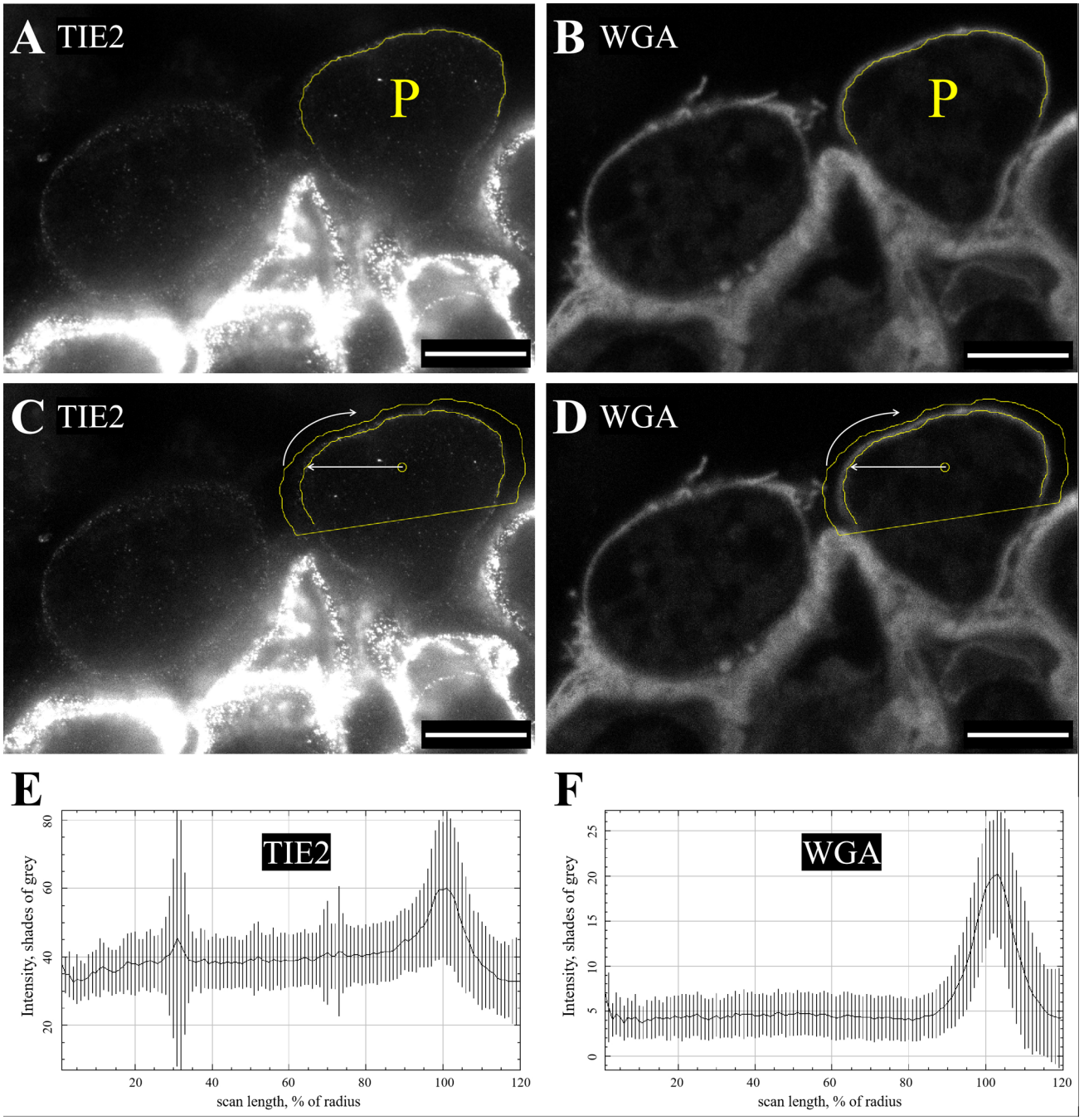

Figure 3. Analysis strategy to determine the maximum signal intensity for the TIE2 and WGA stains on STED images. A, B: Freehand selection over the TIE2 signal (A) expressed on the top of a podocyte cell. The selection was copied via de ROI Manager for the WGA staining image (B); C, D: Clock Scan Combined selected area based on the ROI previously described, for signal intensity measurements on the TIE2 image (C), and WGA image (D). The Clock Scan protocol collects the pixel intensity in a radial manner, starting from the center of the ROI, clockwise, toward the edge of the ROI region (white arrows); E, F: Expression of the gray intensities for TIE2 (E) and WGA (F), measured with the Clock Scan Combined plugin; correction filters applied for the TIE2 channel: Brightness and Contrast—minimum displayed value 19; maximum displayed value 300. P = podocyte; scale bar 5 µm.

(in total, 26 different images over three different experimental replicates were used).

Statistics

A Welch's analysis of variance or *t*-test was used to assess the lifetime measurements between the different signal populations (autofluorescence, nonspecific binding of the secondary antibody, specific TIE2 signal of the blood vessel lumen or podocytes) and the maximum intensity values of the TIE2 and WGA measurements obtained from the Clock Scan analysis. We assumed no significant differences between the various fluorescence lifetimes and no significant differences between the maximum intensity values of the TIE2 signal and those of the cell membranes stained with WGA. A p value lower than 0.05 was considered significant.

Results

Verification of Podocyte Identity and TIE2-Podocin Colocalization Attempts

In initial exploratory experiments, a podocin marker was included to establish correct podocyte localization. Cells located inside the glomerulum, facing the Bowman's space and positioned on top of glomerular capillaries, displayed clear anti-podocin-positive cell bodies. The slit diaphragm also showed the expected podocin staining pattern (Fig. 4). These findings confirmed that the structures analyzed in subsequent experiments corresponded to podocytes.

In an attempt to perform colocalization using the anti-TIE2 and anti-podocin primary antibodies, cross-reactivity between the anti-podocin and the secondary StarRED (normally used against the TIE2 primary) was detected (Fig. 5). Briefly, control experiments and FLIM analysis confirmed that kidney sections stained only with podocin and StarRED displayed signal in the StarRED channel, despite the absence of the anti-TIE2 primary antibody, while the podocin channel remained negative as expected (Fig. 5A to C). This indicates that StarRED antibodies can generate a false-positive signal in the presence of the selected podocin primary antibody. When both TIE2 and podocin antibodies were applied, the StarRED channel showed two distinct lifetime populations, revealing simultaneous true TIE2 labeling and nonspecific StarRED binding to the podocin antibody, rather than lifetime variation of TIE2 in the slit diaphragm. In this experiment, the podocin channel produced one single lifetime population (Fig. 5E, F, and H). This prevented reliable colocalization of TIE2 with podocin and prompted us to focus on cell morphology and cell localization based on the WGA stain as a primary identification method for all the datasets included in this article.

We focused further experiments on staining only with the anti-TIE2 primary, its corresponding StarRED secondary, and the WGA membrane stain. To ensure that the observations were not affected by spectral bleed-through, the spectral profiles associated with the dye combinations used were examined (Fig. 6). No detectable signal was present within the emission peak of the StarRED dye (655 nm) when exciting with the 405 laser used for the WGA dye and expected signal was detected when exciting with the 645 nm laser used for the StarRED dye, confirming that the measurements in this channel were free from spectral bleed-through or contaminating fluorescence species.

However, we noticed a considerable amount of fluorescence coming from the parenchymal tissue in addition to the expected TIE2 stain and this prompted additional investigations into potential nonspecific binding of the antibody panel.

Characterization of Autofluorescence and Antibody Cross-Reactivity to Validate TIE2 Immunostaining

To determine the sources of nonspecific signal and confirm that the TIE2 signal observed on the podocytes was specific, a series of control stains were performed to identify autofluorescence and nonspecific primary or secondary antibody binding.

Primary nonspecific binding was examined by using a control experiment with a recombinant TIE2 protein. After binding with recombinant TIE2, the TIE2 signal in the glomerulum was abolished; however, the primary antibody still stained the parenchyma. This indicates nonspecific binding of the primary antibody to the parenchymal tissue, but specific binding to the TIE2 receptor in the glomerulum (Fig. 7).

We further noted that the secondary antibody contributed to additional nonspecific parenchymal staining. Based solely on fluorescence intensity, the sources of signal could not be reliably separated. Therefore, we employed FLIM to distinguish specific TIE2-associated fluorescence from autofluorescence or nonspecific secondary antibody binding.

The analysis strategy (Fig. 8) contained the following steps: First, in the autofluorescence and secondary-only control datasets, we manually traced ROIs over regions with distinct lifetimes based on morphological patterns observed in the tissue [e.g., red blood cells (RBCs), parenchyma, nonspecific secondary staining]. These lifetime populations were marked on

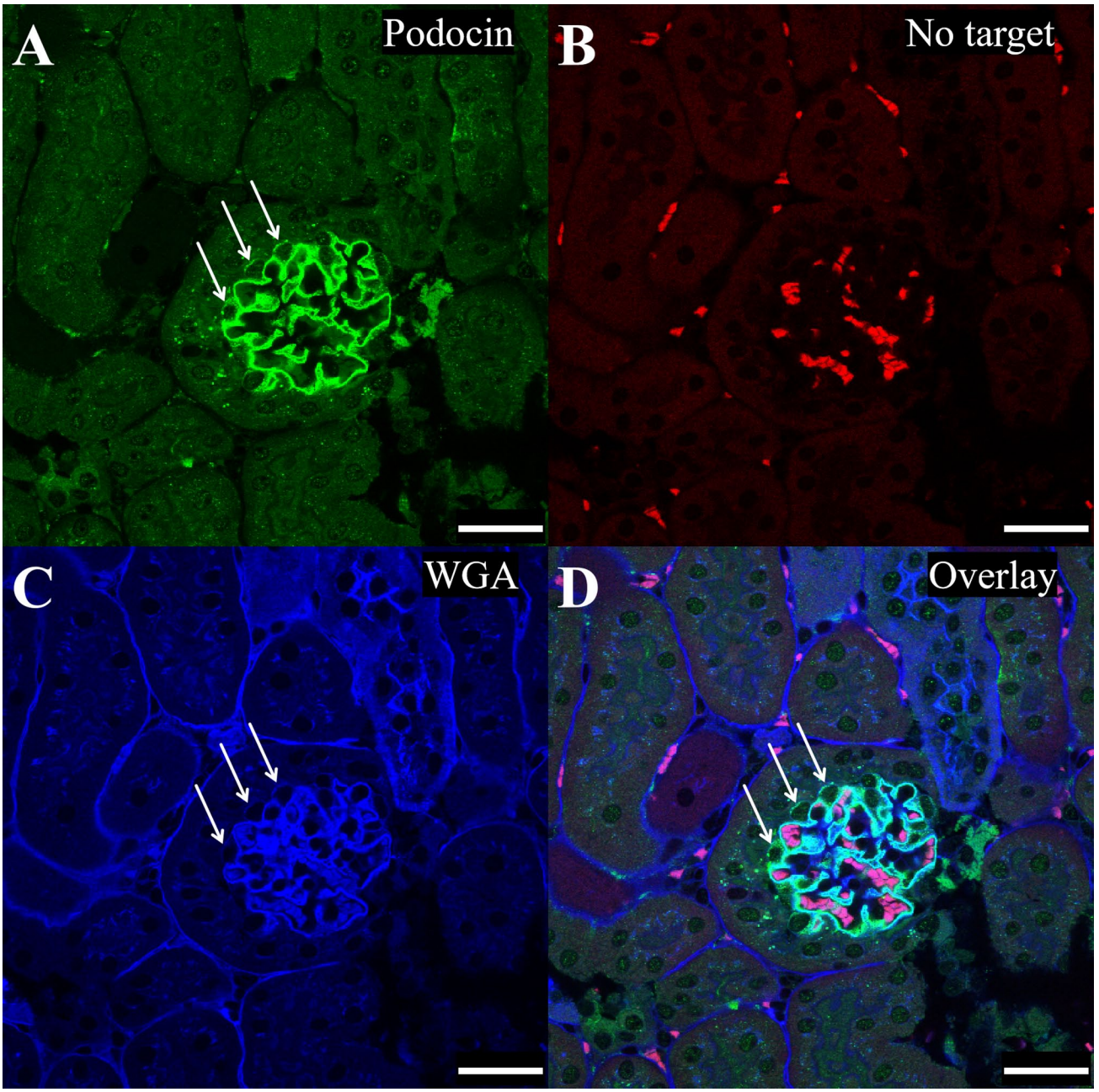

Figure 4. Podocyte localization inside the glomerulum based on immunostaining with podocin. A: Podocytes (tip of white arrowheads) and slit diaphragm stained against podocin (green). B: HyD R detector normally used for TIE2 detection appears with minimal autofluorescence (red) as no target for TIE2 was used; C: Wheat germ agglutinin membrane stain (blue). Tip of the white arrows showcasing the podocyte cells from A. D: Composite of A, B, and C; scale bar 40 µm.

the phasor plots, with yellow for autofluorescence and red for nonspecific binding (Fig. 8A to L). We used the circle tool in the phasor plots to back-gate the autofluorescence and secondary antibody staining to the FLIM images. As the lifetime distribution on the phasor displayed "an elongated shape," multiple circles were traced on the phasor to cover all lifetime species present. To ensure that all lifetime species were accounted for, the regions designated on the phasor plot were determined based on the overlay of all control phasors (per experimental replicate) (Fig. 9). Next, these control-derived cluster coordinates were transferred to the phasor plots of the TIE2-stained samples (Fig. 8S and T). Any signal gated on the podocytes or

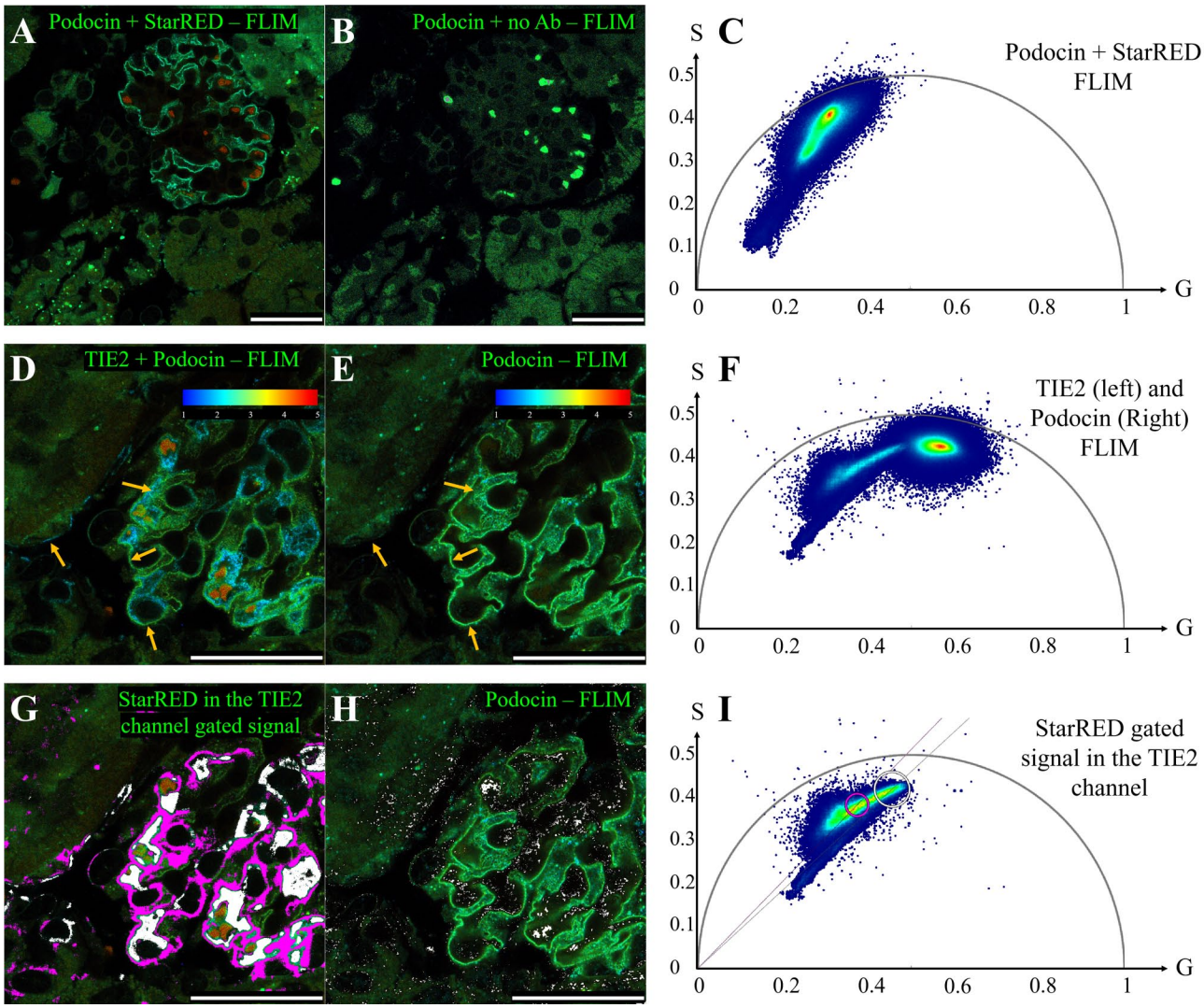

Figure 5. StarRED secondary antibody binds to both anti-TIE2 primary antibody and anti-podocin primary antibody—FLIM. A, B, C: Control experiment using the anti-podocin primary antibody [primary rabbit anti-podocin P0372 (Sigma-Aldrich)] and the Star RED secondary antibody [donkey anti-goat IgG StarRED 638 (Abberior), normally used to bind to the TIE2 primary antibody]. The StarRED secondary antibody in the FLIM channel (HyD R detector) shows immunofluorescent signal despite no primary antibody against TIE2 was used, indicating nonspecific binding of the Star RED secondary antibody to the anti-podocin antibody (A). The HyD X detector (donkey anti-rabbit A-21207 detection channel) shows no visible signal as expected (B). The phasor plot (C) shows the signal population corresponding to the nonspecific binding of the StarRED secondary antibody; D, E, F: Double immunofluorescence staining with primary antibodies against TIE2 and podocin shows two different lifetimes in the StarRED channel, marked in blue and green (yellow arrowheads in D), indicating contributions from both genuine TIE2 signal and nonspecific binding to the podocin antibody, and not a lifetime variation of the TIE2 binding to the slit diaphragm. The podocin FLIM channel shows only one lifetime marked in green (E). The phasor plot (F) shows the signal population corresponding to the StarRED (HyD R detector) and anti-podocin (HyD X detector) secondary antibodies; G, H, I: TIE2 population (white) and podocin population (magenta) (G) corresponding to the StarRED secondary antibody signal, gated on the FLIM image as observed on the phasor plot obtained from the HyD R detector (I). In the podocin FLIM channel (H) negligible signal corresponding to the StarRED marked population can be observed; scale bar 40 μm.

blood vessel areas and falling within the red or yellow control clusters was automatically considered unreliable and excluded from further analysis. We then created ROIs only in podocyte regions that were not marked by these control clusters (Fig. 8O and P), and we compared them with ROIs created inside the blood vessels as internal positive controls for TIE2 staining (Fig. 8M and N). We color-coded these positive signal

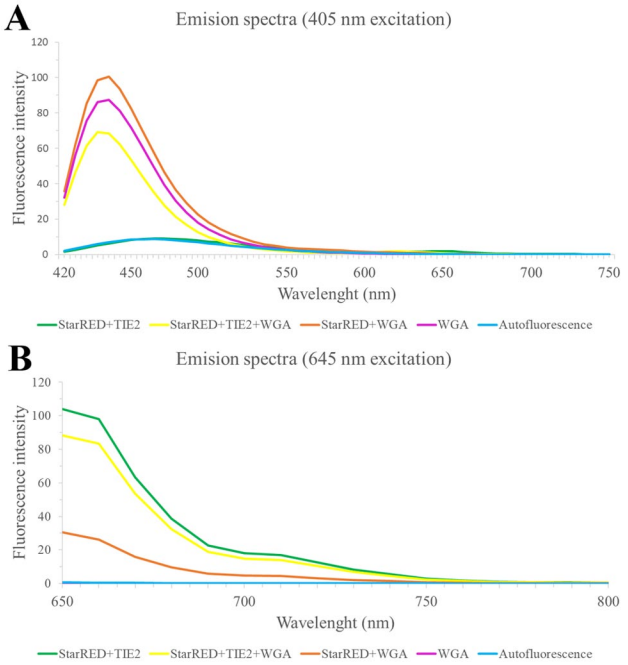

Figure 6. Emission spectra after excitation with 405 and 645 nm lasers. A: Emission spectra of different conditions as acquired post excitation with the 405 nm laser. Samples that contained WGA (yellow, orange, pink) presented with a peak fluorescence intensity around the 450 nm wavelength while the sample not containing the WGA stain (green) only showcased a minimal increase in fluorescence intensity similar to that of the autofluorescent control (blue). While exciting with the 405 laser, no sample showed an intensity increase at around the 650 nm wavelength. This suggests that the 405 laser we use to excite the WGA dye does not affect the StarRED dye, nor does the WGA stain leak in the StarRED spectral channel; B: Emission spectra of different conditions as acquired post excitation with the 645 nm laser. Samples containing the StarRED dye (green, yellow, and orange) showcased an increase in fluorescence intensity at around the 650 nm wavelength and a slow decrease toward the infrared spectrum. Samples not containing StarRED dye (pink and blue) did not show an increase in intensity. This suggests that the 645 nm laser used to excite the StarRED dye does not affect the WGA dye; thus, no interference from this dye can be observed in the StarRED spectral channel.

clusters in white (Fig. 8Q and R). This strategy shows that TIE2-positive podocyte signals were separated from autofluorescence and nonspecific binding.

Data obtained were analyzed using both the phasor plot approach and the fitting approach. The tissue autofluorescence signal was almost completely removed by applying correction thresholds, suggesting that this signal is minimal and negligible. Only the signal coming from within the blood vessels, most likely from the RBC, could not be filtered out. The clusters corresponding to RBCs had an average lifetime of 1.54 ns based on the phasor plot analysis and 1.51 ns based on the fitting approach when considering the amplitude weighted values (Fig. 10 yellow box plots).

For the StarRED nonspecific binding control, we separated the signal into clusters that varied slightly from image to image with an average lifetime of 2.64 ns for phasor or 2.84 ns for the fitting analysis (Fig. 10 red box plots).

Lifetime Populations and Precise Subcellular Localization of the TIE2 Receptor on Mouse Kidney Podocytes

We then used FLIM to identify the specific anti-TIE2 stain on glomerular endothelial cells and podocytes, and STED to determine the precise subcellular localization of the TIE2 receptor on the podocyte cells.

For the FLIM approach, to determine the correct fluorescence lifetime corresponding to the positive TIE2 staining, data were again analyzed using both the phasor plot method and the fitting method. For the phasor plot approach, two clusters of fluorescent signal were identified. The first cluster encompassed the signal coming from the positively stained endothelial cells, with an average lifetime of 1.95 ns (min.: 1.74 ns, max.: 2.18 ns). The second cluster corresponded to the podocyte TIE2 and had an average lifetime of 1.95 ns (min.: 1.74 ns, max.: 2.29 ns). Both clusters followed similar trends on the phasor plot, with the podocyte cluster overlapping the endothelial cell cluster (Fig. 11). Similar results were obtained based on the fitting analysis with lifetime values of 1.90 ns (min.: 1.69 ns, max.: 2.10 ns) for the endothelial cells group and 1.91 ns (min.: 1.65 ns, max.: 2.12 ns) for the podocyte group. The statistical analysis confirmed that there were no significant differences between the values in these two clusters in terms of fluorescence lifetime ($p>0.05$), supporting the theory that the signal observed on the podocytes was indeed coming from the TIE2 protein.

We considered the TIE2 values obtained from the podocytes and from the endothelial cells as one group. To assess the significance of the differences between the values obtained using the phasor plot versus the fitting method, we compared each group (TIE2 signal, nonspecific binding of the secondary antibody control, and autofluorescence control) obtained from the phasor plot analysis with the same group obtained with the fitting analysis (Fig. 10). This analysis yielded similar values for both the phasor plot and the fitting methods for two of the groups. The p values indicate that the TIE2 ($p=0.240$) and autofluorescence ($p=0.724$) measurements were not significantly different when comparing the phasor and fitting methods. However, the nonspecific binding groups showed a statistically

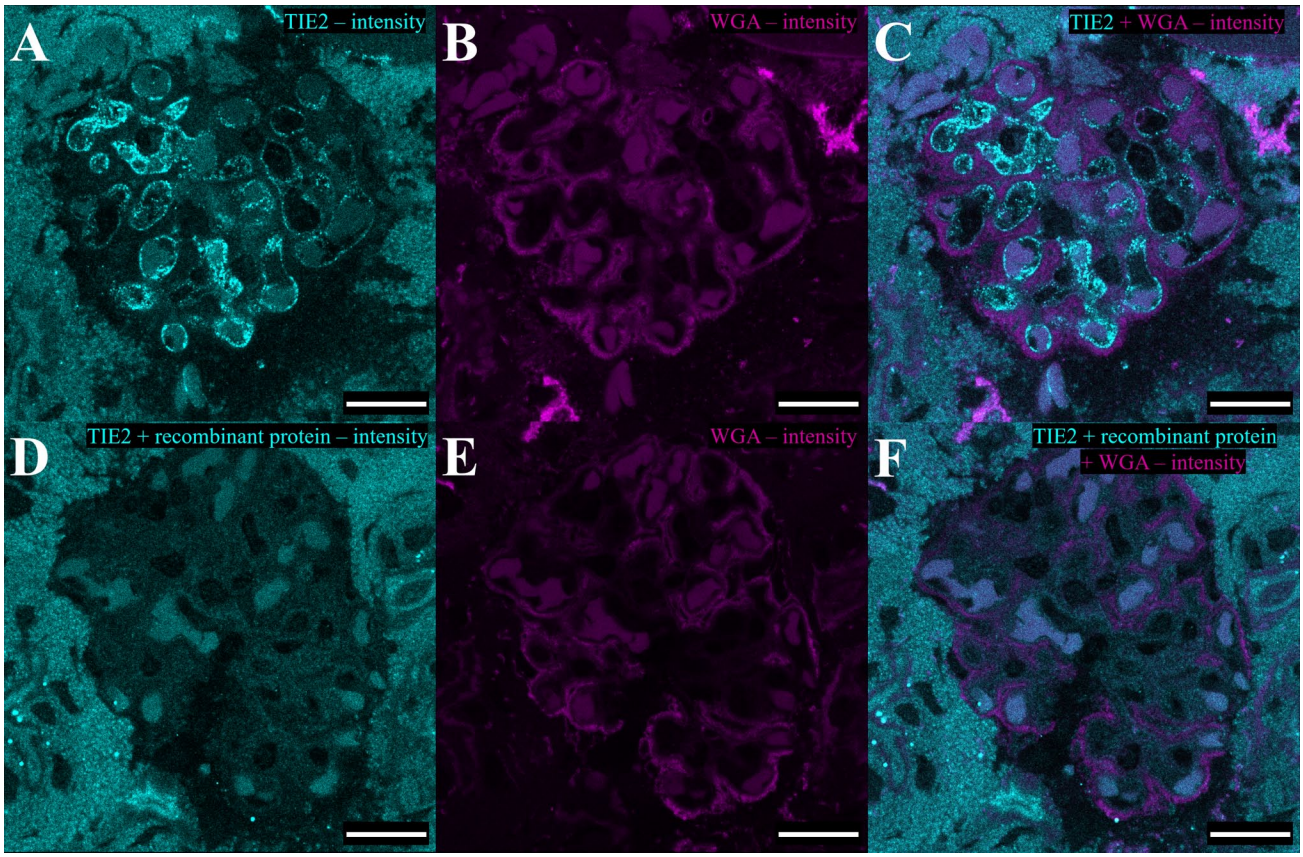

Figure 7. TIE2 staining in the presence or absence of TIE2 recombinant protein. A: TIE2 staining of a kidney glomerulum (intensity image); B: Wheat Germ Agglutinin membrane staining on a kidney glomerulum (intensity image); C: Overlay of A and B; D: TIE2 staining of a kidney glomerulum in the presence of a TIE2 recombinant protein (Recombinant Mouse Tie-2 Fc Chimera Protein, catalog number 762-T2, R&D Systems). In the presence of the recombinant protein, the TIE2 specific signal inside the blood vasculature disappeared. Signal from the parenchyma remained visible, suggesting that the primary antibody binds nonspecific to the tissue and specific to the TIE2 target; E: Wheat Germ Agglutinin membrane stain of a kidney glomerulum (intensity image); F: Overlay of D and E (intensity image); scale bar 20 µm.

significant difference between the phasor plot and the fitting approach (p=0.021). This suggests that the two techniques are best used as complementary as the fitting method can be more sensitive to complex microenvironmental setups.

We then compared the TIE2 group with the nonspecific binding group and the autofluorescence group obtained from the phasor plot. These groups differed significantly from each other (p<0.05), confirming that the signal is distinct and can be separated between the three groups. The same result was obtained when comparing the three groups obtained with the fitting method with a p<0.05. This confirmed that the analysis strategy allowed us to accurately separate the three groups analyzed.

Of note, we observed a decrease in fluorescence lifetime between the positive TIE2-stained clusters and the nonspecific secondary antibody control. To investigate whether this decreased lifetime could be caused by the interactions of the secondary antibody binding to the primary antibody, an in vitro droplet test with only these two antibodies was performed. The overall fluorescence lifetimes were similar when analyzed based on phasor plot and fitting method and were as follows: 3.224 ns (phasor) and 3.108 ns (fitting) for the StarRED 400 µg/ml (Fig. 12A), 2.907 ns (phasor) and 2.796 ns (fitting) for the StarRED bound to the anti-TIE2 antibody 50 µg/ml (Fig. 12B), and 2.497 ns (phasor) and 2.291 ns (fitting) for the StarRED bound to the anti-TIE2 antibody 100 µg/ml (Fig. 12C). This confirms that the protein–protein interaction between the StarRED secondary antibody and the anti-TIE2 primary antibody leads to a decreased overall lifetime measured in the StarRED channel, independent of tissue microenvironment and dependent on the proportions between the two solutions.

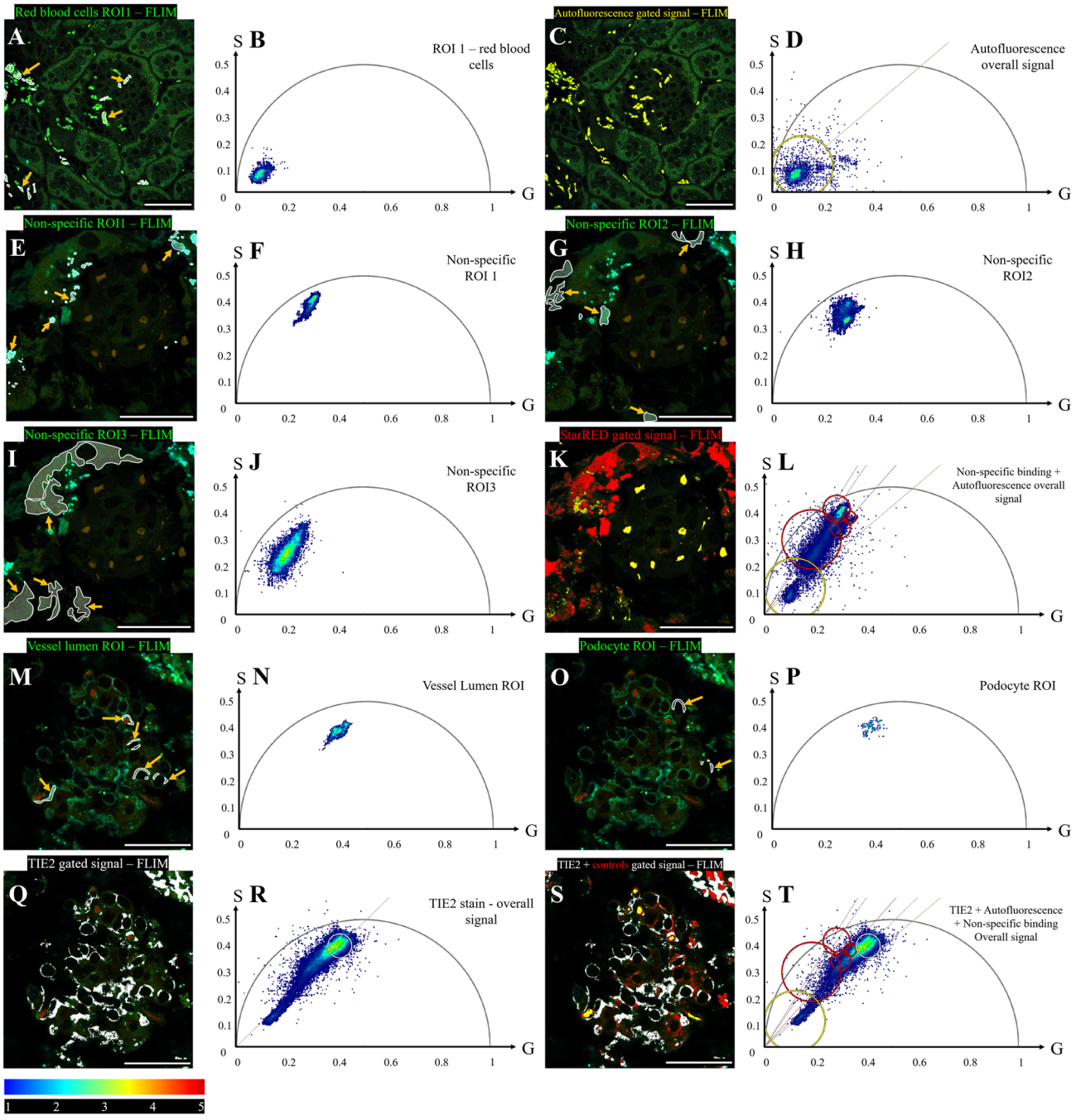

Figure 8. Analysis strategy: determining autofluorescence, nonspecific binding of secondary antibody control and positive staining. A: Fast-FLIM image of tissue autofluorescence in the StarRED spectral channel. ROIs were traced over the red blood cells (RBC) (yellow arrowheads); B: Phasor plot representative for the autofluorescent ROI population determined in A; C, D: Gated autofluorescence of the red blood cells (yellow) (C) as marked on the overall phasor plot (D); E, G, I: Fast-FLIM image of secondary antibody nonspecific binding in the StarRED spectral channel. Different sets of ROIs were traced on the images, each set corresponding to one image (E, G, or I) (yellow arrowheads); F, H, J: Phasor plots representative for the secondary antibody nonspecific binding ROI populations, as traced on their corresponding image (E, G, or I); K, L: Gated nonspecific secondary antibody binding (red) and autofluorescence (yellow) (K) as marked on the overall phasor plot (L); M, O: Fast-FLIM image of TIE2 staining on the StarRED spectral channel. ROIs were traced based on morphological patterns and lifetime color coding over the blood vessel lumen (M) and podocyte cell body (O) (yellow arrowheads) excluding regions marked by the previous mentioned controls; N, P: Phasor plots representative for the vessel lumen TIE2

Figure 8. *(continued)*

ROIs (N) and podocyte TIE2 ROIs (P); Q, R: Gated TIE2 signal population (white) (Q) as observed on the overall phasor plot in panel R; S: TIE2 signal population gated in white, nonspecific binding population gated in red and autofluorescence population gated in yellow on the Fast-FLIM image in the StarRED spectral channel as observed on the overall phasor plot in panel T; T: Phasor plot representing the overall fluorescence lifetime collected for the TIE2-stained samples. White circle delimits the TIE2 lifetime population, red circles determine the nonspecific binding of the secondary antibody populations and the yellow circle delimits the autofluorescent population; for visual aid and for the purpose of this representation only, white lines were traced, post-analysis, over the selected ROI regions; scale bar A, C 60 µm, E, G, I, K, M, O, Q, S 40 µm.

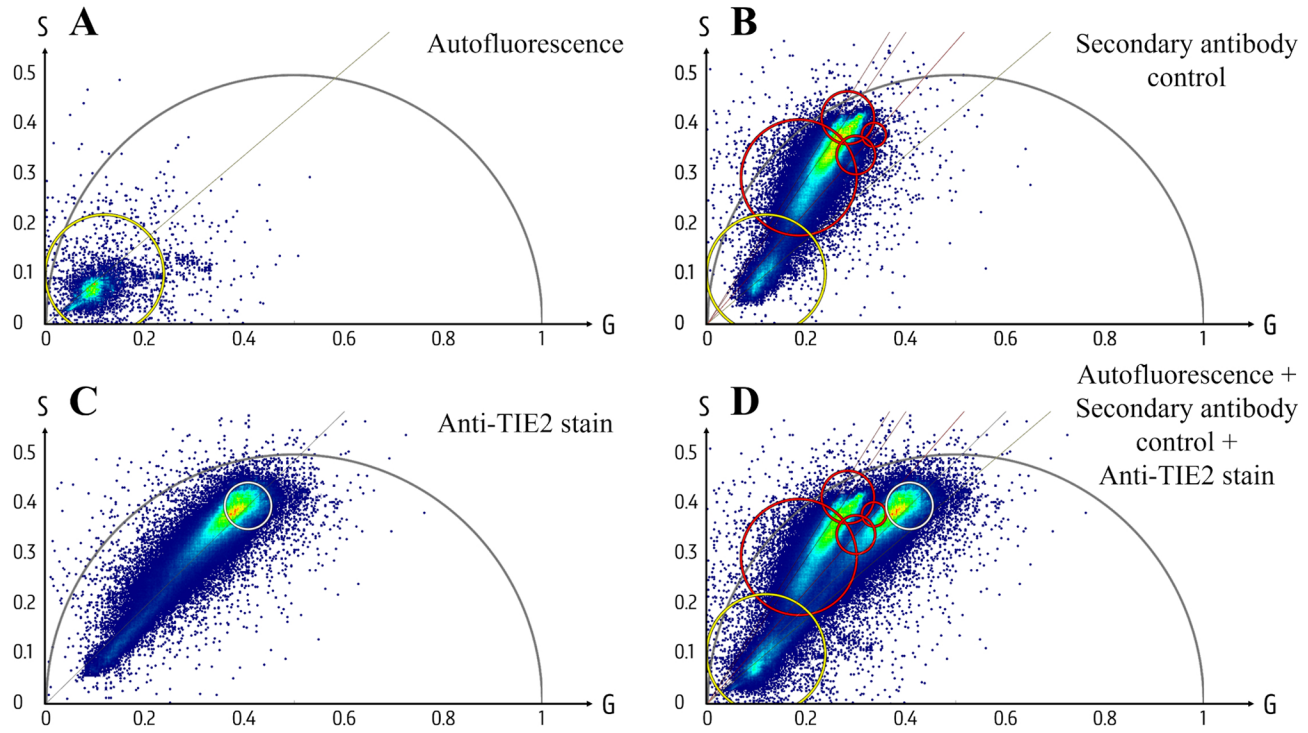

Figure 9. Overlay of multiple phasor plot distribution coordinates of control and positive stained samples. A: Fluorescence lifetime distribution on the phasor plot of the autofluorescence RBC; B: Fluorescence lifetime distribution on the phasor plot of the StarRED secondary antibody control C: Fluorescence lifetime distribution on the phasor plot of the StarRED secondary antibody bound to anti-TIE2 primary antibody; D: Composite of panels A, B, and C. It can be observed from the image that the addition of the primary antibody shifts the overall measured fluorescence lifetime. To obtain the overlay images, all phasor plots analyzed within the experimental replicates were used.

Finally, to precisely define the subcellular localization of TIE2, we analyzed the STED datasets. Using 2D-STED and confocal microscopy, we observed TIE2 signals on the podocytes' cell bodies facing the Bowman's space. The intensity of the TIE2 signal was significantly lower compared with that of glomerular endothelial cells, which were used as positive controls (Fig. 13A to C). Notably, the STED analysis revealed minimal TIE2 staining in some regions of the major foot processes.

To confirm that the TIE2 signal was found on the cell membrane, a Clock Scan analysis (Fig. 3) was used to determine the signal intensity distribution on the podocyte cell body (Fig. 13D to F). Based on this, the maximum signal intensity of both TIE2 and WGA (membrane stain) was consistently plotted at similar distances from the ROI center—100% for TIE2 and 101% for WGA (Fig. 13G). Statistical analysis indicated that there was no significant difference between the values. This overlap supports the conclusion that TIE2 is localized on the podocyte cell surface.

Discussion

In recent years, various methods have emerged to enable deeper analysis of tissues at cellular and subcellular levels. Techniques such as Stochastic Optical Reconstruction Microscopy, Photoactivated Localization Microscopy, and Point Accumulation in Nanoscale Topography offer lateral and axial resolutions ranging from 20 to 50 nm.[17] When coupled with tissue clearing and expansion protocols, STED approaches these

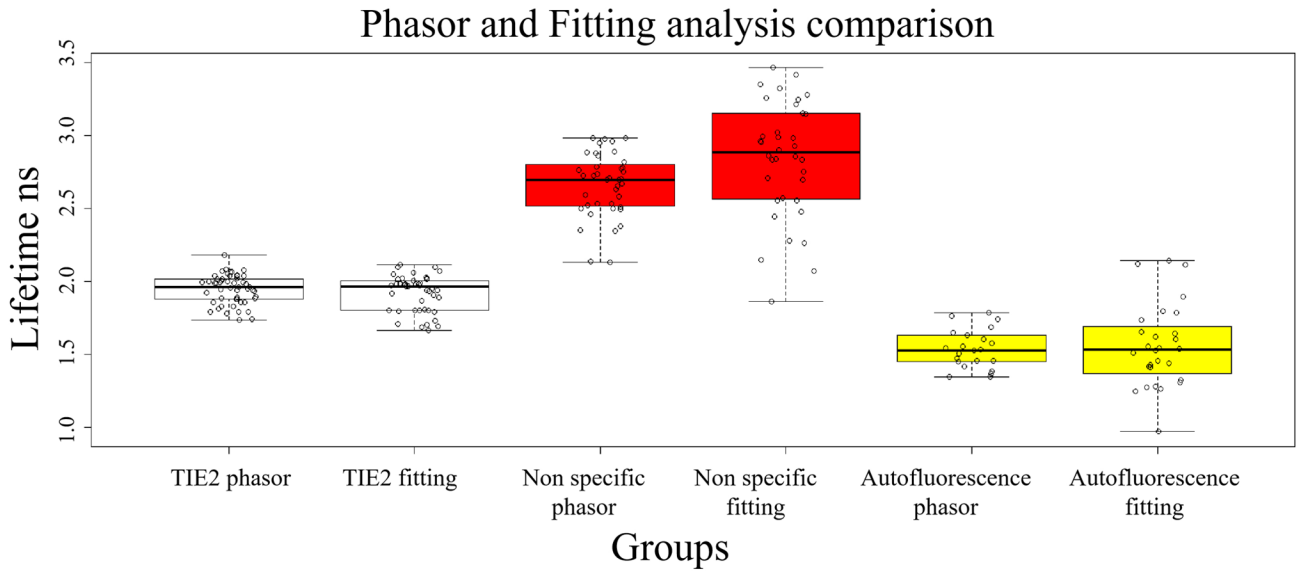

Figure 10. TIE2, autofluorescence, and nonspecific binding of the secondary antibody to the tissue group values comparison. Boxplot comparison of lifetime values obtained using phasor and fitting methods for three different groups: TIE2 signal (white), nonspecific binding of the secondary antibody control (red), and autofluorescence control (yellow).

limits, achieving 30 nm in the x-y plane and 70 nm in the z-plane.[16,17] Although FLIM does not achieve such high resolution, it has significantly affected live confocal and multiphoton microscopy, especially in the fields of cell metabolism or intramolecular interactions (FRET).[22] Notably, FLIM provides an additional layer of information in interpreting fluorescent data, as it helps to distinguish overlapping spectral fluorophores based on their lifetime.[13] STED and FLIM have already been developed a couple of decades ago, but the complex algorithms used for data acquisition and analysis, lack of suitable fluorophores, and the high costs prevented their wide use. This is now rapidly changing, with the development of more automated data analysis solutions, machine learning, and new phasor FLIM analysis methods.[30–33] However, optimal dual STED-FLIM systems of comparable functionality are not yet widely available.

Previous studies focused on the advantages that FLIM brings to STED imaging in terms of increasing the final image resolution.[34] An early study showcased the potential of the dual system as it enabled the visualization of individual actin structures in natural killer cells.[35] Another recent study underscored the advantages of adopting a STED-FLIM approach in multilabeled samples featuring five different fluorophores. Signal separation based on phasor plots demonstrated that the combination of both methods enabled the separation of spectrally similar fluorochromes within the same spectral channel on both confocal and, with greater resolution, STED-acquired images.[36]

Here, we used STED and FLIM individually and correlated the results. STED provided precise target localization, whereas FLIM helped to distinguish specific TIE2 signals from autofluorescence and nonspecific binding of the secondary antibody.

Despite using well-optimized tissue clearing protocols that promote antibody penetration to a depth of 60 µm[16] (Fig. 2), residual tissue autofluorescence and nonspecific secondary antibody binding remained present in our samples (Fig. 8). FLIM allowed us to successfully separate autofluorescence, nonspecific binding to the tissue of the secondary antibodies, and the TIE2-specific signal (Figs. 8 and 11). Additional spectral analysis ("lambda scan") confirmed that there were no interferences from the WGA staining in the StarRED channel (Fig. 6). For the STED images and based on intensity readouts, we could not fully separate the secondary antibody nonspecific binding to the tissue from the positive signal. However, our controls showed lower intensity readouts in the secondary antibody samples compared with the primary antibody-labeled samples, supporting the hypothesis that the secondary antibody binds nonspecifically to the tissue. By correlating this with the data from the FLIM analysis, we interpret that the signal captured with STED in the positively stained samples originated from a specific interaction of secondary antibody to the primary antibody against TIE2. This example highlights the potential advantages of a dual STED-FLIM approach, where FLIM can distinguish between autofluorescence, nonspecific binding, and the specific signal that is accurately localized by

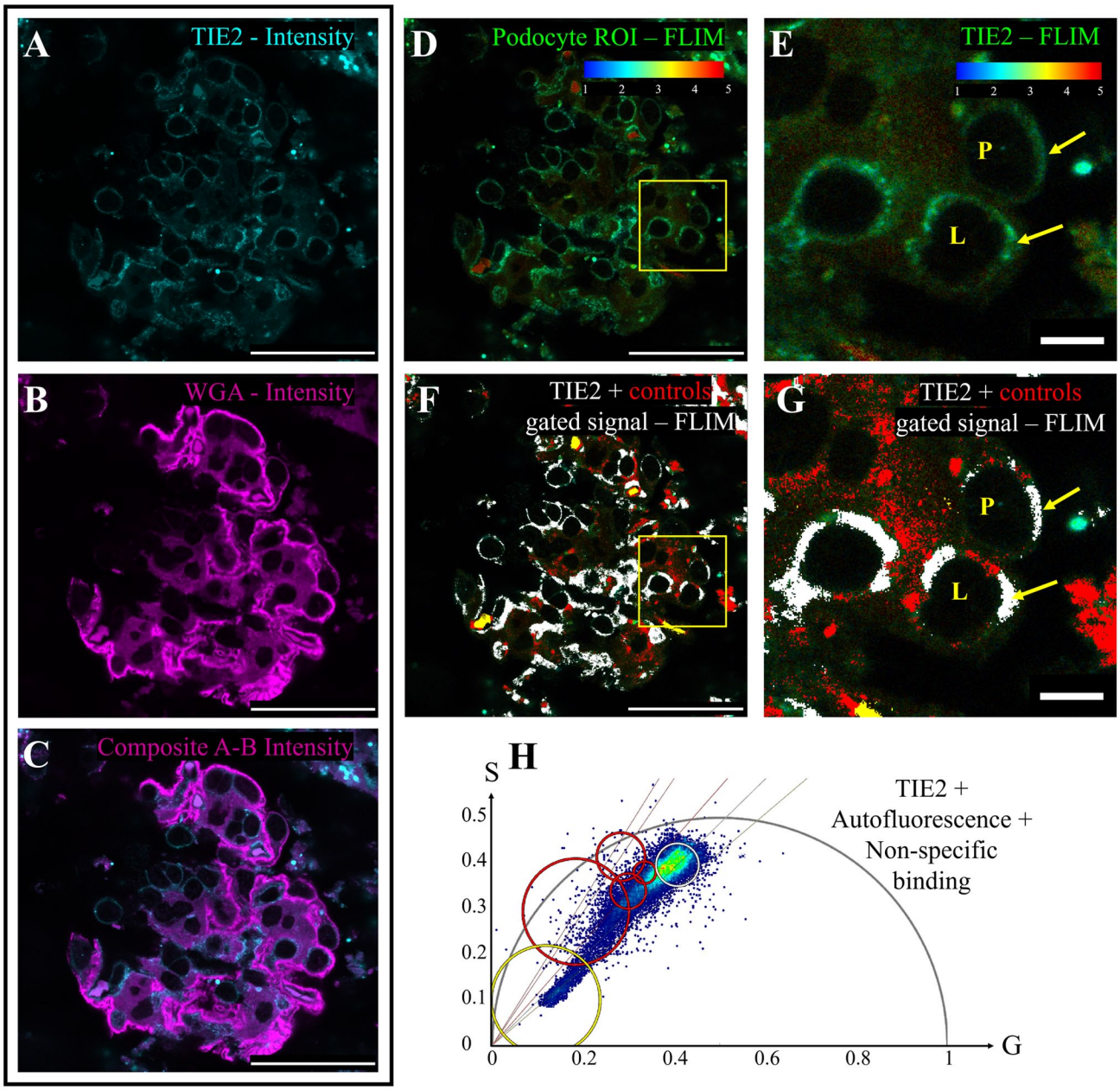

Figure 11. Fluorescence lifetime imaging microscopy reveals specific TIE2 signal in the glomerulus sections. L—vessel lumen; P—podocyte; arrowheads pinpoint at the TIE2 staining; A: TIE2 stain on podocyte and adjacent capillaries (intensity image); B: Wheat Germ Agglutinin membrane staining (intensity image); C: Overlay of A and B (intensity image); D, F: Fast-FLIM image of TIE2 staining (D) and TIE2 + control signals gated on the image (F); E, G: Zoom in from D and F on a podocyte (P) and blood vessel lumens (L) showcasing at the tip of the arrows the TIE2 stain in E and the Gated signal from the phasor plot corresponding to the TIE2 cluster in G. H: Phasor plot of the TIE2 lifetime signal cluster and the region of interest marked in white on the Fast-FLIM images (F and G). The phasor distribution also visualizes nonspecific binding of the secondary antibody (red) and tissue autofluorescence (yellow); scale bar: A, B, C, D, F 40 µm; E, G 5 µm.

STED. It should be noted that within our experimental conditions, potential nonspecific binding of the primary antibody could not be differentiated with FLIM. In positive samples, lifetime values for TIE2 ROIs of blood vasculature and of podocytes were similar to the lifetime values of certain parenchyma ROIs, indicating that the primary antibody binds to TIE2 or to conformationally similar receptors in the parenchyma. We could not detect significant changes in the lifetimes of these areas, indicating that the microenvironment or

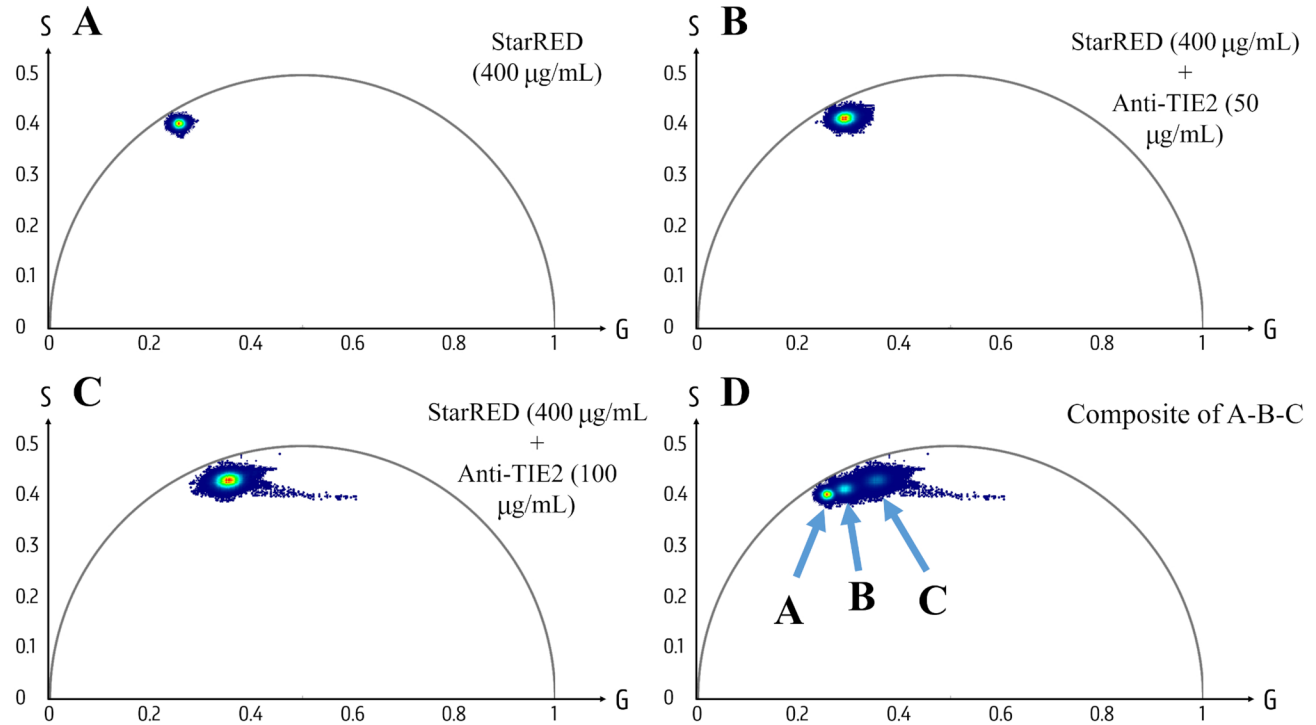

Figure 12. Fluorescence lifetime comparison between StarRED secondary antibody and StarRED bound to primary anti-TIE2 antibody in an in vitro droplet test. A: Fluorescence lifetime distribution on the phasor plot of the StarRED secondary antibody (400 µg/ml); B: Fluorescence lifetime distribution on the phasor plot of the StarRED secondary antibody (400 µg/ml) bound to anti-TIE2 primary antibody (50 µg/ml); C: Fluorescence lifetime distribution on the phasor plot of the StarRED secondary antibody (400 µg/ml) bound to anti-TIE2 primary antibody (100 µg/ml); D: Composite of panel A, B, and C. It can be observed from the image that the addition of the primary antibody shifts the overall measured fluorescence lifetime.

protein–protein interactions do not sufficiently alter fluorescence lifetime to distinguish binding specificity of the primary antibody. To tackle this, a control experiment with a recombinant TIE2 protein was performed that showed primary antibody staining the parenchyma, despite saturation, suggesting nonspecific binding to tissue but specific binding to the TIE2 receptor (Fig. 7).

For the FLIM data measurements, two different methods were used to analyze the cluster signals, namely, the phasor method and the fitting method, and each respective group (TIE2, autofluorescence control and secondary antibody control) was compared with its counterpart (Fig. 10). The analysis showed that for two groups (TIE2 and autofluorescence), there was no significant difference between the values obtained through the phasor plot method versus those obtained through the fitting method. For the third group (secondary antibody nonspecific binding control), the difference was significant between the values obtained with the two methods. This suggests that for a more clear and objective data analysis, both methods should be used together. Although the fitting method is more susceptible to user bias when selecting the decay model, it can capture finer lifetime details coming from more complex heterogeneous decay dynamics, and the phasor plot offers an intuitive overview over the multiple fluorescent populations present in a sample. However, within each method, there was a clear statistically significant difference between the three groups analyzed (TIE2 signal vs. nonspecific binding of the secondary antibody control vs. autofluorescence control), confirming that the cluster groups we analyzed were different and came from separate signal populations.

Our analysis focused on the podocyte cell body, and we employed a method of cell recognition based on cell morphology and localization. In the initial exploratory experiments, anti-podocin was used to identify podocytes. Results showed that the cells facing the Bowman's space and sitting on top of the glomerular tuft were positively stained (Fig. 4). These experiments confirmed correct localization; however, due to the cross-reactivity between the podocin primary and the secondary StarRED (normally used against the TIE2 primary) antibodies (Fig. 5), we decided to focus on cell morphology and localization based on the WGA stain as a primary identification method for all the datasets included in this article.

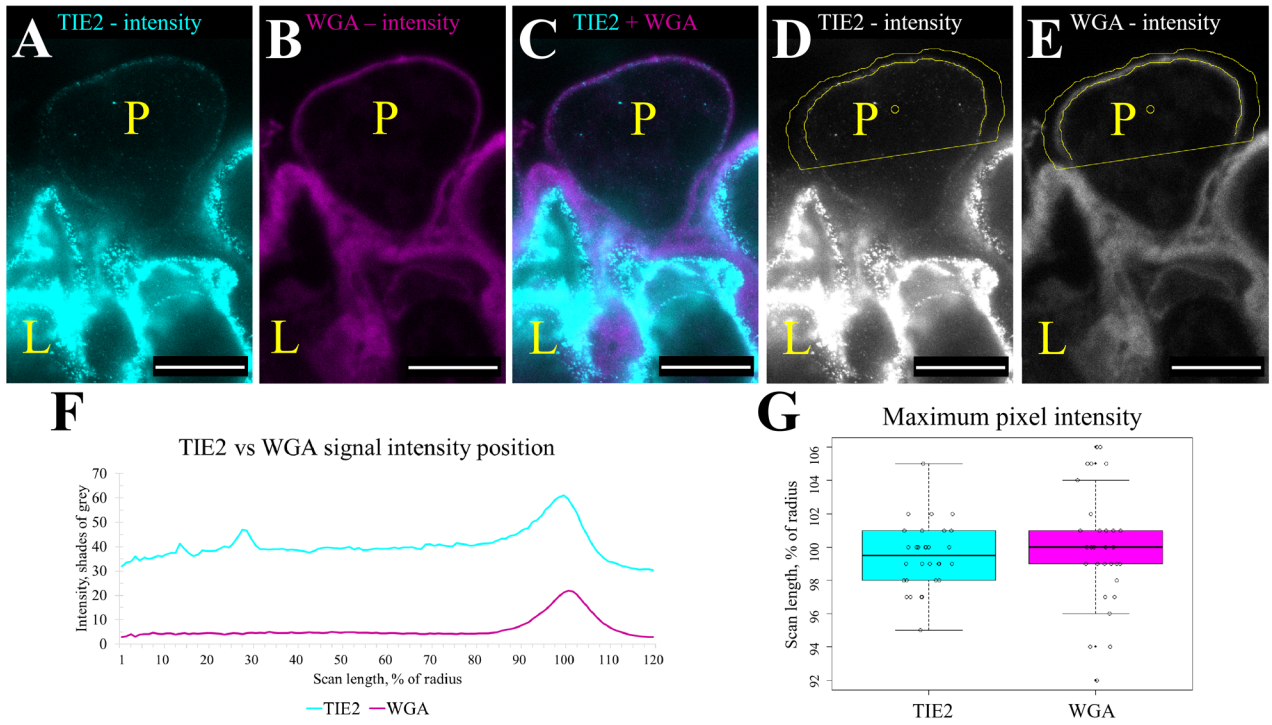

Figure 13. TIE2 localization on glomerular podocytes revealed with STED microscopy. L = vessel lumen; P = podocyte; A, B: Podocyte and adjacent capillary lumen stained against TIE2 (A) and WGA (B); C: Composite of A and B; D, E: TIE2 (D) and WGA (E) staining converted to grayscale, with indicated region for Clock Scan analysis profile (yellow ROI); F: Signal intensity position within the selected area in D and E, measured with the Clock Scan Combined plugin, representing TIE2 (cyan) and WGA (magenta). G: Box plots displaying the position of the maximum pixel intensity values for the TIE2 channel (cyan) and the WGA channel (magenta) from all the measured images; scale bar 5 µm.

While recognizing this as a limitation, due to the specific morphology and localization of the podocytes, especially when using high-resolution microscopy, these cells are quite easily distinguished when located at the periphery of the glomerular tuft and in cross-sections where they appear in a perpendicular orientation toward the blood vessels. Thus, podocin removal did not compromise further analysis strategy.

We found that TIE2 is mainly localized on the cell surface of the podocyte cell body (Fig. 13). Lifetime measurements of ROIs representing podocytes and ROIs representing the glomerular vasculature were statistically similar, strengthening our hypothesis that the TIE2 receptor is predominantly localized on the podocyte cell body. Compared with glomerular endothelial cells and based on fluorescence intensity data, we observed a lower expression of the TIE2 on the podocyte cells. This is consistent with the previous reports, which suggest that TIE2 has lower expression in non-endothelial cells.[4,5,9] Apart from occasional staining in some of the major foot processes of the podocytes, no TIE2 signal was observed in the slit diaphragm. However, due to the correction thresholds applied during analysis, we cannot fully rule out the presence of the TIE2 on the slit structure. Furthermore, WGA was selected for its compatibility with STED imaging and its ability to label the membranes of cells surrounding the capillary lumen. However, it also stains the slit diaphragm and the glomerular basement membrane nonspecifically, which complicates the analysis of these compartments. To confirm the presence or absence of the TIE2 receptor in the slit diaphragm, a counterstain with a slit diaphragm marker such as podocin should be performed. In our experiment, the nonspecific binding of the StarRED secondary antibody normally used against TIE2 to the podocin primary complicated this approach. Additional podocyte markers such as synaptopodin or Wilms' Tumor 1 (WT1) or a different podocin marker could also be used to confirm colocalization on the cell body and to strengthen the podocyte identification strategy. The use of secondary antibodies spectrally and chemically distinct from those employed here could represent a viable alternative. However, the Abberior dyes possess superior fluorophore labeling, making them ideal for STED imaging even at the expense of decreased binding specificity within our experimental conditions.

The presence of the TIE2 receptor on mouse podocytes prompts for future research of the functionality of the receptor in these cells. The TIE2 ligands are part of the angiopoietin family with angiopoietin 1 and angiopoietin 2 being the most widely studied. In pericytes, angiopoietin 1 stimulation results in increased cellular survival upon tumor necrosis factor-alpha–induced apoptosis and increased cell migration. On the contrary, angiopoietin 2 increases apoptosis but does not interfere with pericyte migration.[4] As podocytes are considered to be pericyte-like cells, we speculate that these ligands can potentially influence the podocytes through the TIE2 receptor, making the angiopoietin-TIE system an interesting target for treatment for various podocytopathies.

Our findings contribute to the limited body of literature supporting the presence of the TIE2 receptor on podocytes. Although seemingly lower expressed compared with endothelial cells, the presence of the TIE2 on podocytes warrants further investigation of its functions in these cells. Understanding these interactions may provide new insights into podocyte biology and the broader mechanisms of kidney function and disease.

Our study also highlights potential advantages of correlating STED and FLIM. With STED's increased resolution and FLIM's lifetime parameter, a dual system combining these two techniques could improve the pitfalls of common autofluorescence staining and allow for a better interpretation of fluorescent signals from low-expressed targets, even in challenging conditions such as thick (100 µm) optically cleared kidney samples, with high background fluorescence and limited antibody availability.

Acknowledgments

Our group wishes to express our sincere gratitude to Dr. David Unnersjö-Jess for his involvement in the early stages of this project as well as for his comments on the manuscript.

Competing Interests

The authors declared no potential conflicts of interest with respect to the research, authorship, and/or publication of this article.

Author Contributions

IAD, IAO, and HDK designed experiments and performed data acquisition; IAD performed experiments, data analysis, data interpretation, and drafted the manuscript; IAO, HDK, WDS, and RID provided insight into data analysis and data interpretation; WDS, RID, PC, IAO, and HDK revised the manuscript; WDS, RID, and PC were involved in initial project conception and design of the overall study.

Funding

The authors disclosed receipt of the following financial support for the research, authorship, and/or publication of this article: This work was supported by the Research Foundation Flanders (FWO) grants I001922N and I012020N, the BOF project grants 01CD11823 and BOF.COR.2022.0003.01, and the Mobility and Sabbatical Funds of Ghent University.

ORCID iDs

Iulia-Aneta Dénes https://orcid.org/0000-0001-9490-7583

Irina A. Okkelman https://orcid.org/0000-0002-7014-6887

Herlinde De Keersmaecker https://orcid.org/0000-0002-3454-6437

Pieter Cornillie https://orcid.org/0000-0003-4412-3427

Ruslan I. Dmitriev https://orcid.org/0000-0002-0347-8718

Ward De Spiegelaere https://orcid.org/0000-0003-2097-8439

Data Availability

Figures and images presented in the manuscript are representative for the datasets. Upon request, additional figures can be made available by contacting Prof. Dr. Ward De Spiegelaere at Ward.DeSpiegelaere@UGent.be.

Literature Cited

1. Dumont DJ, Gradwohl G, Fong GH, Puri MC, Gertsenstein M, Auerbach A, Breitman ML. Dominant-negative and targeted null mutations in the endothelial receptor tyrosine kinase, TEK, reveal a critical role in vasculogenesis of the embryo. Genes Dev. 1994;8:1897–909.
2. Saharinen P, Eklund L, Miettinen J, Wirkkala R, Anisimov A, Winderlich M, Nottebaum A, Vestweber D, Deutsch U, Koh GY, Olsen BR, Alitalo K. Angiopoietins assemble distinct TIE2 signalling complexes in endothelial cell-cell and cell-matrix contacts. Nat Cell Biol. 2008;10(5):527–37.
3. Leppänen VM, Saharinen P, Alitalo K. Structural basis of TIE2 activation and TIE2/TIE1 heterodimerization. Proc Natl Acad Sci U S A. 2017;114:4376–81.
4. Cai J, Kehoe O, Smith GM, Hykin P, Boulton ME. The angiopoietin/TIE-2 system regulates pericyte survival and recruitment in diabetic retinopathy. Invest Ophthalmol Vis Sci. 2008;49(5):2163–71.
5. Teichert M, Milde L, Holm A, Stanicek L, Gengenbacher N, Savant S, Ruckdeschel T, Hasanov Z, Srivastava K, Hu J, Hertel S, Bartol A, Schlereth K, Augustin HG. Pericyte-expressed TIE2 controls angiogenesis and vessel maturation. Nat Commun. 2017;8:16106.
6. Venneri MA, De Palma M, Ponzoni M, Pucci F, Scielzo C, Zonari E, Mazzieri R, Doglioni C, Naldini L. Identification of proangiogenic TIE2-expressing monocytes (TEMs) in human peripheral blood and cancer. Blood. 2007;109:5276–85.
7. Liu D, Martin V, Fueyo J, Lee OH, Xu J, Cortes-Santiago N, Alonso MM, Aldape K, Colman H, Gomez-Manzano C. TIE2/TEK modulates the interaction of glioma and brain

tumor stem cells with endothelial cells and promotes an invasive phenotype. Oncotarget. 2010;1(8):700–9.
8. Kitajima D, Kasamatsu A, Nakashima D, Miyamoto I, Kimura Y, Saito T, Suzuki T, Endo-Sakamoto Y, Shiiba M, Tanzawa H, Uzawa K. TIE2 regulates tumor metastasis of oral squamous cell carcinomas. J Cancer. 2016;7(5):600–7.
9. Logothetidou A, De Spiegelaere W, Van den Broeck W, Vandecasteele T, Couck L, Simoens P, Cornillie P. Stereological and immunogold studies on TIE1 and TIE2 localization in glomeruli indicate angiopoietin signaling in podocytes. Micron. 2017;97:6–10.
10. Satchell SC, Harper SJ, Tooke JE, Kerjaschki D, Saleem MA, Mathieson PW. Human podocytes express angiopoietin 1, a potential regulator of glomerular vascular endothelial growth factor. J Am Soc Nephrol. 2002; 13(2):544–50.
11. Williams DB, Carter CB. Transmission electron microscopy. Boston: Springer US; 2009.
12. Winey M, Meehl JB, O'Toole ET, Giddings TH. Conventional transmission electron microscopy. Mol Biol Cell. 2014;25:319–23.
13. Hato T, Winfree S, Day R, Sandoval RM, Molitoris BA, Yoder MC, Wiggins RC, Zheng Y, Dunn KW, Dagher PC. Two-photon intravital fluorescence lifetime imaging of the kidney reveals cell-type specific metabolic signatures. J Am Soc Nephrol. 2017;28(8):2420–30.
14. Zhang Y, Wang Y, Cao WW, Ma KT, Ji W, Han ZW, Si JQ, Li L. Spectral characteristics of autofluorescence in renal tissue and methods for reducing fluorescence background in confocal laser scanning microscopy. J Fluoresc. 2018;28(2):561–72.
15. Sicherre E, Favier AL, Riccobono D, Nikovics K. Nonspecific binding, a limitation of the immunofluorescence method to study macrophages in situ. Genes (Basel). 2021;12:649.
16. Unnersjö-Jess D, Butt L, Höhne M, Witasp A, Kühne L, Hoyer PF, Patrakka J, Brinkkötter PT, Wernerson A, Schermer B, Benzing T, Scott L, Brismar H, Blom H. A fast and simple clearing and swelling protocol for 3D in situ imaging of the kidney across scales. Kidney Int. 2021;99(4):1010–20.
17. Ranjit S, Lanzanò L, Libby AE, Gratton E, Levi M. Advances in fluorescence microscopy techniques to study kidney function. Nat Rev Nephrol. 2021;17(2):128–44.
18. Wunderlich LCS, Ströhl F, Ströhl S, Vanderpoorten O, Mascheroni L, Kaminski CF. Superresolving the kidney—a practical comparison of fluorescence nanoscopy of the glomerular filtration barrier. Anal Bioanal Chem. 2021;413(4):1203–14.
19. Unnersjö-Jess D, Scott L, Blom H, Brismar H. Super-resolution stimulated emission depletion imaging of slit diaphragm proteins in optically cleared kidney tissue. Kidney Int. 2016;89(1):243–7.
20. Huang B, Babcock H, Zhuang X. Breaking the diffraction barrier: super-resolution imaging of cells. Cell. 2010; 143:1047–58.
21. Lauterbach MA, Eggeling C. Foundations of STED microscopy. In: Fornasiero EF, Rizzoli SO, editors. Super-resolution microscopy techniques in the neurosciences. Totowa, NJ: Humana Press; 2014. p. 41–71.
22. Dmitriev RI, Intes X, Barroso MM. Luminescence lifetime imaging of three-dimensional biological objects. J Cell Sci. 2021;134:1–17.
23. Okkelman IA, Zhou H, Borisov SM, Debruyne AC, Lefebvre AEYT, Zoccoler ML, Chen L, Devriendt B, Dmitriev RI. Visualizing the internalization and biological impact of nanoplastics in live intestinal organoids by fluorescence lifetime imaging microscopy (FLIM). Light Sci Appl. 2025;14(1):272.
24. Colyer RA, Lee C, Gratton E. A novel fluorescence lifetime imaging system that optimizes photon efficiency. Microsc Res Tech. 2008;71(3):201–13.
25. Schindelin J, Arganda-Carreras I, Frise E, Kaynig V, Longair M, Pietzsch T, Preibisch S, Rueden C, Saalfeld S, Schmid B, Tinevez J-Y, White DJ, Hartenstein V, Eliceiri K, Tomancak P, Cardona A. Fiji: an open-source platform for biological-image analysis. Nat Methods. 2012;9:676–82.
26. Dobretsov M, Petkau G, Hayar A, Petkau E. Clock scan protocol for image analysis: ImageJ plugins. J Vis Exp. 2017;124:55819.
27. Digman MA, Caiolfa VR, Zamai M, Gratton E. The phasor approach to fluorescence lifetime imaging analysis. Biophys J. 2008;94:L14–6.
28. Stringari C, Cinquin A, Cinquin O, Digman MA, Donovan PJ, Gratton E. Phasor approach to fluorescence lifetime microscopy distinguishes different metabolic states of germ cells in a live tissue. Proc Natl Acad Sci U S A. 2011;108:13582–7.
29. Pelet S, Previte MJ, Laiho LH, So PT. A fast global fitting algorithm for fluorescence lifetime imaging microscopy based on image segmentation. Biophys J. 2004;87(4): 2807–17.
30. König K. Brief history of fluorescence lifetime imaging. In: König K, editor. Multiphoton microscopy and fluorescence lifetime imaging: applications in biology and medicine. Berlin: De Gruyter; 2018. p. 3–16.
31. Vicidomini G, Bianchini P, Diaspro A. STED super-resolved microscopy. Nat Methods. 2018;15:173–82.
32. Cunha I, Latron E, Bauer S, Sage D, Griffié J. Machine learning in microscopy—insights, opportunities and challenges. J Cell Sci. 2024;137(20):jcs262095.
33. Vallmitjana A, Torrado B, Durkin AF, Dvornikov A, Rajil N, Ranjit S, Balu M. GSLab: open-source platform for advanced phasor analysis in fluorescence microscopy. Bioinformatics. 2025;41(4):btaf162.
34. Wang L, Chen B, Yan W, Yang Z, Peng X, Lin D, Weng X, Ye T, Qu J. Resolution improvement in STED super-resolution microscopy at low power using a phasor plot approach. Nanoscale. 2018;10:16252–60.
35. Lenz MO, Brown ACN, Auksorius E, Davis DM, Dunsby C, Neil MAA, French PMW. A STED-FLIM microscope applied to imaging the natural killer cell immune synapse. Proc SPIE. 2011;7903:79032D.
36. Gonzalez Pisfil M, Nadelson I, Bergner B, Rottmeier S, Thomae AW, Dietzel S. Stimulated emission depletion microscopy with a single depletion laser using five fluorochromes and fluorescence lifetime phasor separation. Sci Rep. 2022;12:14027.